THE JOURNAL OF PHYSICAL CHEMISTRY C
A JOURNAL OF THE AMERICAN CHEMICAL SOCIETY

pubs.acs.org/JPCC

Article

From Self-Affine Ag to Mounded $Ag@Ag_2O$ Core–Shell Nanoplasmonic Surfaces By Sonochemistry

Biljana Pejova,* Simona Premcheska, and Emel Sherif Miftar

Cite This: *J. Phys. Chem. C* 2023, 127, 11204–11217

Read Online

ACCESS | Metrics & More | Article Recommendations | Supporting Information

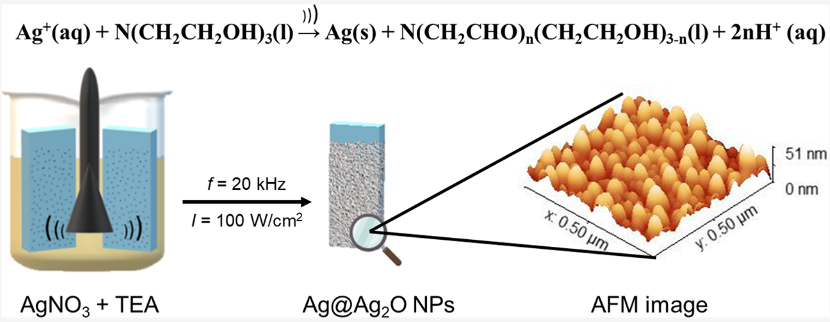

ABSTRACT: A controllable ultrasound-assisted synthetic approach has been developed that allows deposition of elemental silver and core–shell $Ag@Ag_2O$ nanoparticles, close-packed in thin-film form on glass substrates, suitable for a wide range of applications. Ultrasonic irradiation modifies the reaction mechanism, allowing precise control over the composition of the nanoparticles and their packing in the form of thin films. The crystal radii of the synthesized materials fall within the nano range (~9 nm in the case of bare Ag, 5 nm for the Ag core, and 9 nm for the Ag_2O shell in the case of $Ag@Ag_2O$ films). Nanostructured Ag films exhibit self-affine, while the films built up by $Ag@Ag_2O$ core–shell nanocrystals exhibit a mounded morphology. The interface width and the mean roughness are significantly smaller for sonochemically synthesized surfaces. The observed trends in the localized surface plasmon resonance (LSPR) absorptions in the case of bare Ag plasmonic surfaces are dominated by the particle size, inhomogeneous broadening induced by the size dispersion of the nanoparticles, interparticle plasmon coupling, and nanocrystal–substrate interaction. The notable red shift of the LSPR absorption maximum in the case of films built up by $Ag@Ag_2O$ core–shell nanoparticles is governed by the influence of the dielectric shell.

1. INTRODUCTION

Metal nanoparticles (NPs) exhibit unique size-dependent properties that are substantially different from those of their bulk counterparts, which makes these systems tremendously significant from the viewpoint of their applicative potential. In this context, the optical properties of metal NPs are among the most important features and they have been of scientific interest for centuries, at least since Michael Faraday's research related to colloidal gold in the middle of the 1800s. Concerning the optical properties of metal NPs, the effect of localized surface plasmon resonance (LSPR)[1,2] is one of the most important phenomena, which acts as a driving force motivating researchers to implement it in a wide range of applications ranging from medical diagnostics[3,4] to nano-optics.[5,6] The LSPR phenomenon derives from coherent oscillations of the conduction band electrons of metal NPs induced by interaction with the electromagnetic field. Upon reducing the dimension of metal NPs below the wavelength of interacting electromagnetic waves, optical properties become dominated by surface plasmons.

The contemporary science of metal NPs is targeted toward development of new, controllable methods for their synthesis with well-defined sizes and shapes without aggregation, as well as with new instrumental tools for investigation of single metal NP properties. Surface plasmons are strongly dependent on the size and shape of the metal NPs, as well as on their dielectric environment.[7] This finding has opened the possibility for modification of optical properties of metal NPs and their tailoring according to the potential need in the context of application. One of the most effective ways of modification of the properties of a metal nanoparticle is to cover its surface with a thin layer of a dielectric material, which leads to creation of a core–shell NP.

Received: February 23, 2023
Revised: May 15, 2023
Published: June 2, 2023

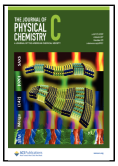

https://doi.org/10.1021/acs.jpcc.3c01267

Core−shell nanostructures are highly functional materials whose properties depend on core and/or shell materials, which may be quite different in terms of physical and/or chemical properties. Due to their modified/improved properties, core−shell NPs have been widely used in many different areas: biomedical and pharmaceutical applications, catalysis, electronics, enhancing photoluminescence, creating photonic crystals, etc.[8−16] In addition to already mentioned applications, core−shell nanostructures have also been used as a template for preparation of nano and micronized hollow particles, which have, on the other hand, found application as micro-vessels, catalytic supports, adsorbents, light-weight materials, isolators, etc.[16] Some of the most interesting contemporary applications have been directed toward surface-enhanced Raman scattering (SERS), shell-isolated NP-enhanced Raman scattering (SHINERS), and tip-enhanced Raman scattering (TERS) functionalities.[17−21]

The focus of the present study is on plasmonic bare silver NPs, as well as on Ag@Ag_2O core−shell nanostructures close-packed in thin-film form. The number of published studies related to core−shell NPs composed of bare Ag and Ag_2O is quite significant, which is a certain indication of the relevance of this system from both fundamental and applicative points of view. What is worth noting, however, is the relatively modest number of studies reporting synthetic routes to Ag@Ag_2O core−shell nanostructures [[12] and references therein], which is quite indicative of the complexity of this task. The existing methods have been based on either laser ablation technique[19,20] or dropwise addition of silver salt to mixture of alcohol and alkali metal hydroxide. The last approach, however, allows merely for synthesis of core−shell NP powders.

Extending our previous research efforts directed toward development of controllable ultrasound-assisted solution growth methods for deposition of nanostructured thin films with tunable properties,[22,23] in the present study, we report a novel highly controllable synthetic route to nanoplasmonic surfaces composed of bare Ag as well as Ag@Ag_2O core−shell NPs. In contrast to the existing synthetic methods in the literature,[12,24,25] we achieve the final aim *not* by intervention in the reactor composition but *merely* by implementing ultrasonic irradiation thereof. We demonstrate that, due to a series of substantial changes in the reaction mechanism introduced by the high-intensity ultrasound, an alternative reaction channel opens up. Consequently, instead of the nanoplasmonic surface built up by bare silver NPs, in the ultrasound-irradiated reaction system, the substrate surface ends up covered with a three-dimensional array of close-packed Ag@Ag_2O plasmonic nanocrystals assembled in thin-film form. Not only the chemical composition of the product but also the overall morphology of the surface are altered—from self-affine to mounded. LSPR absorption properties undergo significant changes as well. We rationalize the observed trends in terms of several separate contributions, accounted for by the modified Mie's theory.

The applicative potential of the obtained Ag@Ag_2O core−shell nanostructures is tremendously high and spans a range of rather heterogeneous areas: optical switching devices, optical data storage systems, antibacterial and antiviral applications, catalysis, oxygen nanosensors,[24−26] and multifunctional substrates for SERS applications.[17−21]

2. EXPERIMENTAL SECTION

Thin films of Ag@Ag_2O core−shell NPs were synthesized using an ultrasound-assisted colloidal approach. The reaction system was prepared using silver nitrate ($AgNO_3$) as a metal ion precursor and triethanolamine, $(CH_2OHCH_2)_3N$ (TEA), with a double role: (i) as a reducing agent and (ii) as a ligand. Sonication of the reaction system was achieved by direct immersion of a home-made ultrasonic probe. Generated ultrasonic irradiation was characterized by frequency of 20 kHz and intensity of 100 W/cm^2.

The developed synthetic procedure includes three steps: (i) treatment of substrates (i.e., microscopic glasses with standard dimensions), (ii) preparation of a colloidal reaction system, and (iii) thin-film deposition process. The substrates were treated following a procedure described in our previous articles devoted to development of semiconductor thin-film deposition methods.[22,27] Briefly, the microscopic glasses (previously well-cleaned with a powerful oxidizing agent—chromosulfuric acid) were treated with 0.03% solution of tin(II) chloride and annealed at 200°C for about a quarter of an hour. The immersion in a diluted solution of $SnCl_2$ leads to formation of stochastically distributed Sn(OH)O nuclei on the substrate surface and their transformation to SnO nanocrystals during the annealing process. This step of the experimental procedure provides chemical modification of the glass surface and results in its improved adhesion properties, which is of essential importance for deposition of high-quality, homogenous thin-film materials. In the next step, the colloidal reaction system was prepared starting with 6 mmol $AgNO_3$, adding an appropriate quantity of TEA and double-deionized water to a total volume of 100 cm^3. TEA was added in excess, so the initially formed precipitate of silver oxide was completely dissolved. As discussed later in the manuscript, aside from complexing agent properties, TEA also manifests certain reduction properties. In the beginning of the reaction, however, as a consequence of the very small concentration of the Ag^+ ions, the redox potential of $Ag^+|Ag$ is significantly diminished, which, in turn, diminishes the reduction properties of TEA as well (see the Supporting Information). In this phase, TEA thus acts dominantly as a complexing agent.

The process of thin-film deposition occurred at around 40 °C and resulted in adsorption and close-packing of formed NPs on the substrate surface. Throughout this step, the colloidal solution was exposed to ultrasonic irradiation generated by an ultrasonic probe, directly immersed therein. In addition to the sonochemical approach, the described experimental procedure was implemented in lack of ultrasonic irradiation of the reaction system, so that the chemical composition and properties of thin films of NPs prepared by both approaches (sonochemical and chemical) could be compared.

Structural, morphological, and optical properties of the synthesized thin films were characterized using several techniques: X-ray diffraction (XRD), atomic force microscopy (AFM), and UV−vis spectroscopy. XRD measurements were performed to prove the chemical identity of deposited materials and to estimate several relevant structural parameters, such as lattice constants, strain, and particle size of obtained nanostructures. XRD patterns were recorded on an Ultima IV X-ray diffractometer (Rigaku Co.) using Cu Kα radiation in the $2\theta/\theta$ scanning mode and a step scan of $\Delta(2\theta) = 0.02°$.

AFM images of the prepared thin films were measured using a Shimadzu Co. SPM model 9600. Imaging was performed in dynamic (i.e., tapping) mode and height, amplitude, and phase images were recorded. The measurements were carried out using an AFM tip whose nominal resonance frequency and force constant are 320 kHz and 42 N/m, correspondingly. The scan rate was 2 Hz, while the images are characterized with a resolution of 512 lines per scan direction. All samples included in the study were scanned at least at a few points. The obtained AFM images were processed and analyzed using the software package Gwyddion.[28] Basic data processing subsequent to image acquisition included just flattening without any additional steps. The flattening procedure was carried out by fitting of the acquired data to a polynomial function of the form

$$P(x, y) = \sum_{j=0}^{m} \sum_{k=0}^{n} a_{j,k} x^j y^k \tag{1}$$

(where n and m denote the horizontal and vertical polynomial degrees, respectively) and subsequent subtraction of the corresponding background representation. Further data analyses included calculation and analysis of first- and second-order statistical parameters as well.

The optical properties were studied by UV–vis electronic spectroscopy. Transmittance spectra were recorded on a Cary 50 spectrophotometer (HP Co.) in a spectral range from 300 to 1100 nm using a glass substrate (with chemically modified surface) as a background. The recorded "raw" transmittance spectra were processed as explained further in the manuscript to construct the corresponding absorption spectra. These were further analyzed and modeled in the context of interpretation of properties dominated by the LSPR effect.

3. RESULTS AND DISCUSSION

3.1. Chemistry and Sonochemistry of the Deposition Process of Silver-Based NP Thin Films. Deposition of silver-based NPs on the substrate surface, followed by formation of a homogeneous thin film, derives from both homogeneous and heterogeneous nucleation processes, which initially occur inside the bulk liquid phase and on the liquid/substrate boundary. The developed method is highly tunable and provides formation of either bare silver NPs (Ag NPs) or silver–silver oxide core–shell NPs ($Ag@Ag_2O$ NPs). The first reaction channel is enabled when the reaction system is not subjected to ultrasonic irradiation, while the second one takes over under conditions that include sonication of the system.

To understand the prevalence of either of the two possible reaction channels and thus to explore further the possibilities for tuning of the product properties, it is essential to get an in-depth insight into the fundamental chemistry of the employed reaction system. From a chemical point of view, there are few relevant, competitive processes, which take place in the reaction system in the presence of TEA. It can act as (i) a hydroxide ion precursor, (ii) a reducing agent, and (iii) a tridentate ligand. All these processes influence the equilibrium concentration of silver(+) cations in the reaction system. The role of TEA as a source of hydroxide ions is due to the process of its hydrolysis:

$$\begin{aligned} &N(CH_2CH_2OH)_3\ (l) + H_2O\ (l) \\ &\quad \leftrightarrows [HN(CH_2CH_2OH)_3]^+\ (aq) + OH^-\ (aq) \end{aligned} \tag{2}$$

The previous equilibrium is left-shifted ((K_b = 5.8 × 10^{-7})[29]), which provides a sufficient quantity of dissolved (non-protolyzed) TEA, which acts as a ligand, forming complex species with silver(+) ions.

The hydroxide ions generated by eq 2 form an unstable silver hydroxide (with K_{sp} = 1.52 × 10^{-8} at 20 °C[29])

$$AgOH\ (s) \leftrightarrows AgOH\ (aq) \leftrightarrows Ag^+\ (aq) + OH^-\ (aq) \tag{3}$$

which readily transforms to a more stable silver oxide:

$$\begin{aligned} &2AgOH\ (s) \leftrightarrows Ag_2O\ (s) + H_2O\ (l) \\ &\quad (pK = 2.875 \text{ at } 25^\circ C\ [29]) \end{aligned} \tag{4}$$

(where $pK = -\log K$ for the equilibrium (4)). In addition to these processes, which strictly control the equilibrium concentration of Ag^+ (aq) in the reaction solution, the reducing properties of TEA[29,30] are of crucial importance for formation of silver-based NPs:

$$\begin{aligned} &2Ag^+\ (aq) + N(CH_2CH_2OH)_3\ (l) \\ &\quad \rightarrow 2Ag\ (s) + N(CH_2CHO)(CH_2CH_2OH)_2\ (l) \\ &\qquad + 2H^+\ (aq) \end{aligned} \tag{5}$$

This redox reaction leads to supersaturation of the reaction system with respect to the main product (Ag) and eventually results in formation of thin films of bare Ag NPs on the substrate surface.

The described chemistry of the deposition process corresponds to experimental conditions under which the reaction system is not influenced by ultrasonic irradiation. However, considering the fact that in this study the main focus is put on thin films of core–shell NPs ($Ag@Ag_2O$), the fundamental question that has to be raised is what happens in the reaction system on a fundamental/molecular level when it is exposed to ultrasound irradiation.

In agreement with the results obtained from the XRD method (discussed in more detail in the following section), it is obvious that the reaction mechanism undergoes some important changes under conditions when the used colloidal system is exposed to ultrasonic irradiation. Since the developed method uses a non-volatile metal precursor ($AgNO_3$) and relatively volatile solvents (water and TEA), the secondary sonochemistry plays an important role. Essentially, the extreme local experimental conditions, introduced by high-intensity ultrasonic irradiation, lead to processes of sonolysis of water and TEA molecules within the vapor phase formed inside the collapsing bubbles. This results in generation of highly reactive species, which diffuse throughout the liquid phase.[31] The processes, which take place inside the bubbles, can be described in the following way:

$$H_2O \rightarrow H\cdot + OH\cdot \tag{6}$$

$$H\cdot + H\cdot \rightarrow H_2 \tag{7}$$

$$H\cdot + OH\cdot \rightarrow H_2O \tag{8}$$

$$OH\cdot + OH\cdot \rightarrow H_2O_2 \tag{9}$$

$$RH\ (\text{volatile vapor}) \rightarrow R\cdot + H\cdot \tag{10}$$

The highly reactive $H^\cdot$ and $OH^\cdot$ radicals further react with TEA in the bulk liquid phase and induce a dramatical increase of reduction rate (compared with a situation when the ultrasonic irradiation is not used) and lead to formation of Ag NPs:

$$\mathrm{RH} + \mathrm{OH}\cdot \rightarrow \mathrm{R}\cdot + \mathrm{H_2O} \tag{11}$$

$$\mathrm{RH} + \mathrm{H}\cdot \rightarrow \mathrm{R}\cdot + \mathrm{H_2} \tag{12}$$

$$\mathrm{Ag^+} + \mathrm{R}\cdot \rightarrow \mathrm{Ag^0} + \mathrm{R^+} \tag{13}$$

$$\mathrm{Ag^+} + \mathrm{H}\cdot \rightarrow \mathrm{Ag^0} + \mathrm{H^+} \tag{14}$$

$$m\,\mathrm{Ag^0} \rightarrow \mathrm{Ag}_m \tag{15}$$

Aside from these processes, one of the additional products of primary sonochemistry (which takes place inside the bubbles) is hydrogen peroxide. Considering the chemistry of this compound,[29] it possesses redox properties, which depend on the pH of the medium:

$$\begin{aligned}\mathrm{H_2O_2}\ (\mathrm{aq}) &+ 2\,\mathrm{H^+}\ (\mathrm{aq}) + 2\,\mathrm{e}\\ &\rightarrow 2\,\mathrm{H_2O}\ (\mathrm{l})\ E^\circ\\ &= +1.78\ \mathrm{V}\end{aligned} \tag{16}$$

$$\mathrm{H_2O_2}\ (\mathrm{aq}) \rightarrow \mathrm{O_2}\ (\mathrm{g}) + 2\,\mathrm{H^+}\ (\mathrm{aq}) + 2\,\mathrm{e}\ E^\circ = -0.70\ \mathrm{V} \tag{17}$$

According to the equations of these redox half-reactions, having in mind that the exploited reaction system is alkaline, H_2O_2 behaves as a stronger reducing than oxidizing agent, providing conditions for growth of Ag NPs. However, a small amount of released hydrogen peroxide (as a result of primary sonochemistry) in the reaction system might participate in secondary sonochemistry (taking place in a bulk liquid) leading to oxidation of the silver NP surface to a silver oxide thin shell and creation of core−shell NPs of $Ag@Ag_2O$ type. Since primary sonochemistry and secondary sonochemistry do not occur when the reaction system is not influenced by high-intensity ultrasonic irradiation, the formation of core−shell NPs is entirely hindered under these circumstances.

Considering the ultrasound-assisted route, in addition to sonochemical effects, physical effects (such as intense shock waves and high-speed jets), induced by cavitation, also play a significant role in the process of formation of NPs, especially in the context of their size, size distribution, and way of their assembling on the substate surface. As it will be discussed in more details in the section related to morphological characterization, the experimental results, obtained by AFM, proved that sonication of the reaction system substantially modifies the morphological properties of the prepared thin films and provides a spherical shape of the deposited core−shell NPs, changes the dispersion of their size distribution, and allows a unique way of close-packing on the substrate surface.

Having in mind the relevance of the self-assembly phenomenon to both fundamental physical chemistry and materials science and technology, in this context, we briefly analyze the possible driving forces leading to organization of the synthesized materials into aggregates and their subsequent deposition on the substrate surface.[32−34] In the case of presently studied materials, the basic mechanism generating a thermodynamic driving force toward self-assembly involves several modes of interaction between the NPs, which differ in both underlying physics and strength. The most important of these interaction modes are (i) dipolar interactions between metal NPs (taking place because of the dipole moment arising as a consequence of ill-defined/ambiguous crystal facets, the non-stationarity of the surface structure, doping, and other structural distortions) or between the capping ligands; in our case, it is TEA that acts as a capping ligand—its presence in the films could be detected by Raman spectroscopy; (ii) van der Waals interactions between the metal NPs or the capping ligands, which arise due to inherent quantum fluctuations of the electronic densities thereof and, although of a short-range character, can sometimes be comparable in strength to the long-range ones; (iii) other electrostatic interactions (such as interactions between charged NPs or charged capping ligands); (iv) hydrogen bonding interactions between capping ligands, which have a hybrid electrostatic + charge transfer character; (v) metallophilic (i.e., argentophilic in the present case) interaction, which arises because of the weak attractive forces between the electrons in a d^{10} or d^8 system; (vi) the amphiphilicity of the TEA acting as a capping ligand; and (vii) confinement of the NPs motion at the glass−solution interface, resulting in the reduction of the freedom of the translational motion. As the method developed in the present study is template-free, the template-directed self-assembly mechanism is not relevant, and the same conclusion holds for other external factor-directed mechanisms (e.g., light-triggering).

According to our experiments, the formation of the core−shell $Ag@Ag_2O$ NPs is very sensitive to the ratio of initial quantities of the two used precursors (TEA vs $AgNO_3$). The optimal ratio, which leads to deposition of high-quality thin films of $Ag@Ag_2O$ NPs, is 2.5:1.

3.2. Structural Considerations Based on XRD Measurements.

3.2.1. Identification of Synthesized Phases. Both obtained materials, relevant to the previously described reaction mechanisms, crystalize in the cubic crystal system. Silver has an *fcc* crystal structure, while the silver oxide lattice is constructed by two intertwined Ag face-centered cubic and O body-centered cubic sublattices. Figure 1a shows that all

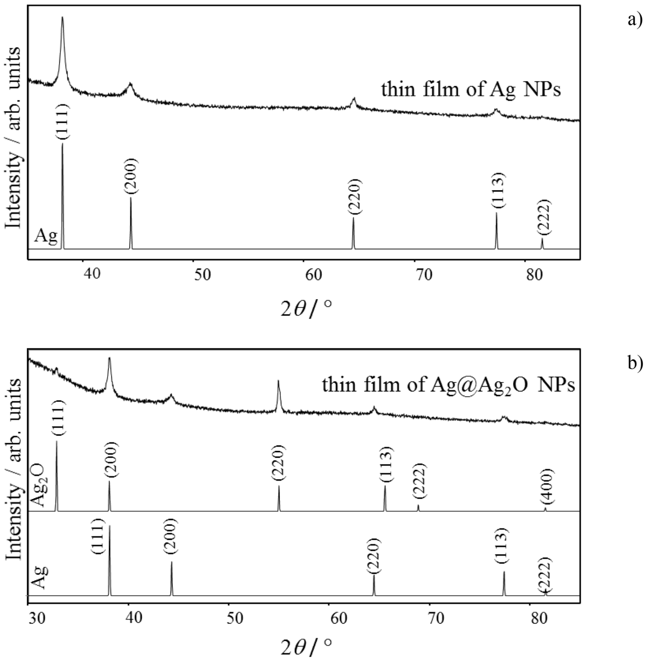

Figure 1. XRD pattern of a thin film specimen of (a) Ag NPs and (b) $Ag@Ag_2O$ core−shell NPs.

expected allowed reflections from cubic silver, i.e., (111), (200), (220), (222), and (311), are present in the XRD pattern of the thin-film specimen from the reaction system, which has not been influenced by ultrasonic radiation. The second XRD pattern (Figure 1b) corresponds to a thin-film specimen prepared under sonication of the reaction system. In addition to the allowed reflections from the *fcc* cubic silver lattice, two additional maxima were observed, which correspond to diffraction from the (111) and (220) planes of the silver oxide lattice. Comparing the experimental and generated XRD patterns (for silver and silver oxide from the crystallographic database[35]) and considering the results related to optical properties (which will be discussed later in the text), it is obvious that NPs obtained under sonication of the reaction system (Figure 1b) are of core−shell type with a silver oxide shell and a silver core. Also, the ratio between intensities of XRD peaks at ∼32 and 55° (corresponding to the (111) and (220) diffracted waves in the case of the silver oxide lattice) implies that the domains inside the Ag_2O shell show a preferred orientation along the [220] crystallographic direction (in the sense of partial alignment of the corresponding planes parallel to the substrate surface).

3.2.2. Crystal Size Estimation. The average size of NPs (in spherical approximation) was estimated using two theoretical approaches based on to some extent different concepts: the Scherer's and Williamson−Hall's.[36−38] To reach this goal, the relevant parameters, which characterize the shapes of the observed XRD peaks (the diffraction angle corresponding to the position of the peak maximum and the full width of the peak at half maximum—β), were estimated applying a least-square non-linear fitting procedure. The fitting was performed by representing the shape of each peak with a linear combination of Gaussian and Lorentzian functions. The obtained values for $\beta_{\text{exp.}}$ were corrected, taking into account the instrumentally induced broadening of diffraction peaks $\beta_{\text{instr.}}$, in line with the following equation:

$$\beta = \sqrt{\beta^2_{\text{exp.}} - \beta^2_{\text{instr.}}} \tag{18}$$

where β is the corrected XRD peak broadening. However, having in mind the pronounced low-dimensional character of obtained materials, our results showed that the contribution of instrumental broadening to the cumulative broadening of XRD peaks is insignificant (i.e., less than 1%).

In order to obtain statistically significant values for the average radius of Ag NPs, a relevant number of measured XRD patterns were processed and the following dependences were constructed: $\cos\theta$ vs $1/\beta$ and $\beta \cos\theta$ vs $\sin\theta$. These plots are given in the Supporting Information. The first dependence derives from the Scherrer's approach, while the second one is in accordance with the Williamson−Hall's approach. Within Scherrer's concept,[37] the slope (a) of the dependence (whose intercept is 0) is related to the average diameter of NPs (d) in line with the following equation:

$$a = K\,\lambda/d \tag{19}$$

where K is Scherrer's constant and λ is the wavelength of used radiation (Cu $K\alpha_1$). The estimated average radius of Ag NPs according to this approach was found to be 9.17 ± 0.35 nm (Table 1).

According to the Williamson−Hall's approach, the average diameter of NPs is related to the intercept (b) of the $\beta \cos\theta$ dependence on $\sin\theta$:

Table 1. Size and Lattice Strain of Ag NPs According to Scherrer's and Williamson−Hall's Approaches

Scherrer's approach	Williamson−Hall's approach	
r (nm)	r (nm)	ε (%)
9.17 ± 0.35 nm	9.03 ± 0.32 nm	$1.08 \times 10^{-1} \pm 7.83 \times 10^{-4}$

$$\beta \cos\theta_{hkl} = 4\varepsilon \sin\theta_{hkl} + \frac{K\lambda}{d} \tag{20}$$

where K and λ have the same meaning as in the context of Scherrer's equation. The estimated average radius of Ag NPs was found to be 9.03 ± 0.32 nm within the framework of this approach. Therefore, it could be concluded that there is an excellent agreement between the average radii values estimated according to the two used concepts.

The slope of $\beta \cos\theta$ on $\sin\theta$ dependence (i.e., $a = 4\varepsilon$), on the other hand, is related to the lattice strain, which is responsible for additional peak broadening (aside from the small particle size). In this context, we define the strain as $\Delta a/a_0$, where a_0 denotes the lattice constant value for bulk Ag while Δa is the change in the lattice constant in the NPs. The estimated value of ε in the case of thin films of bare Ag NPs, according to the Williamson−Hall's approach, is $1.08 \times 10^{-1} \pm 7.83 \times 10^{-4}$%. Since the estimated peak position parameters corresponding to the XRD maxima are insignificantly shifted with respect to the bulk microstrain-free sample (the shifts being smaller than 0.1° on the 2θ scale in the case of all XRD peaks), it has been concluded that Ag NPs are characterized by a minor non-uniform lattice strain, i.e., the strain field contains both compressive and tensile components. This is in accordance with the estimated value for the lattice strain.

As the diffraction peak at ∼38° could be due to the presence of both silver and silver oxide phases, only XRD maxima, which correspond to diffraction angles of ∼55 and ∼44°, were used for estimation of the geometrical characteristics of core−shell $Ag@Ag_2O$ NPs. Therefore, in the framework of Scherrer's concept, the radius (r_2), estimated applying the fitting procedure of the XRD peak at ∼55°, is 14.12 ± 0.81 nm, while using the experimental data related to XRD peak, which appears at ∼44°, the estimated radius of the silver core is (r_1) is 4.89 ± 0.23 nm. On the basis of estimated data, it can be concluded that the estimated value of Ag_2O shell thickness ($r_2 - r_1$) is ∼9.22 nm.

To get better insights into the reproducibility of the developed synthetic methods, as well as to explore whether there are significant differences between the colloidal chemical and sonochemical approaches reflecting in the actual average NP sizes in different samples and the sensitivity of these values to the experimental conditions, we have represented the measured data series for a number of samples synthesized by both methods with the so-called violin plots, along with the more standard box plots. Violin plots extend the advantages offered by box plots by addition of the data probability density, smoothed by a kernel density estimator. They are exceptionally useful when it is needed to compare the distribution of a given variable across some categories. Figure 2 shows the box plots and violin plots of the average crystal sizes obtained from a series of different samples synthesized by colloidal chemical and ultrasonically supported approaches.

In contrast with the other cases that have been studied by our group so far,[22,23,27] in the current study, sonication of the reaction system creates NPs with a larger average size

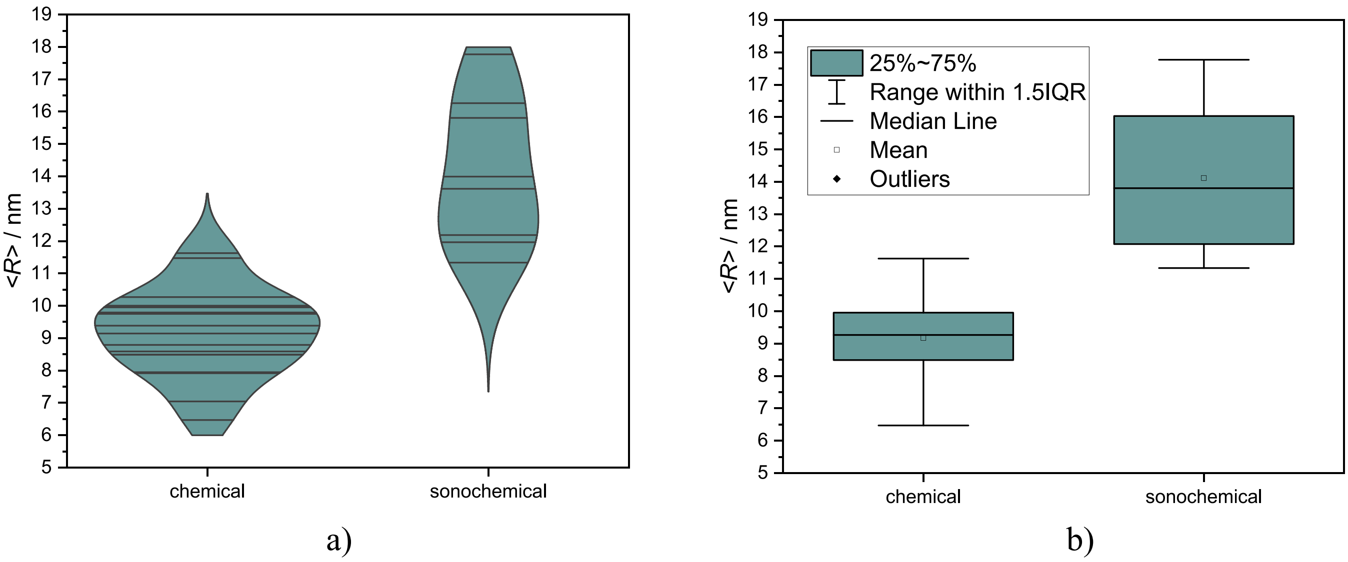

Figure 2. Violin (a) and box (b) plots of the average crystal sizes obtained from a series of different samples synthesized by colloidal chemical and ultrasonically supported approaches.

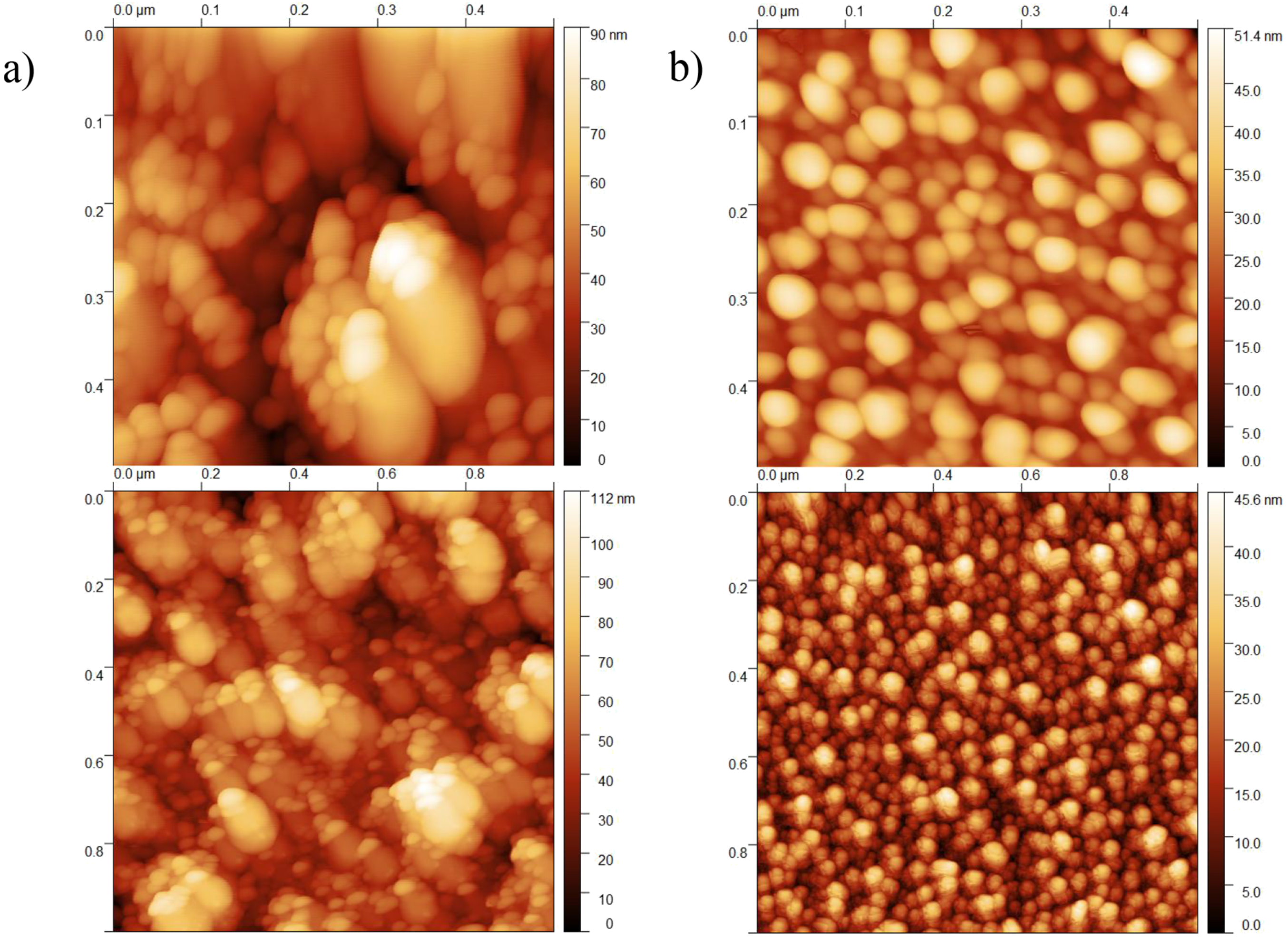

Figure 3. AFM images of thin films of bare Ag NPs (a) and core−shell Ag@Ag_2O NPs (b).

deposited in thin-film form. Under most circumstances, such observation could mean that the collision of the highly energized NPs as a consequence of the shockwaves and microjets, generated under heterogeneous sonochemistry conditions, exhibit collisions in which the released energy can lead to local overheating and sequential melting of the NPs, resulting in their agglomeration and hence larger crystal size. However, in the present case, sonication of the reaction system fundamentally changes the reaction mechanism, leading to growth of the $Ag@Ag_2O$ core−shell NPs. Therefore, we here deal with a sonochemically supported growth of the oxide shell surrounding the initially grown Ag NPs.

3.3. AFM Measurements: Evidence for Ultrasonic Influence on the Self-Assembly Process of Ag and $Ag@Ag_2O$ NPs and Their Shape and Size Distribution. Additional confirmation for the nano size of the synthesized particles, deposited on a substrate surface, was obtained using AFM. Figure 3a shows AFM images of a thin-film specimen composed of close-packed bare Ag NPs (with scanning areas of 500 nm × 500 nm and 1 μm × 1 μm), while Figure 3b corresponds to AFM images of a thin-film sample of $Ag@Ag_2O$ core−shell NPs. According to the obtained results, Ag NPs and $Ag@Ag_2O$ NPs have a distinctive way of self-assembling on the substrate surface. $Ag@Ag_2O$ NPs are more closely packed and have a specific way of ordering as noticed in Figure 4.

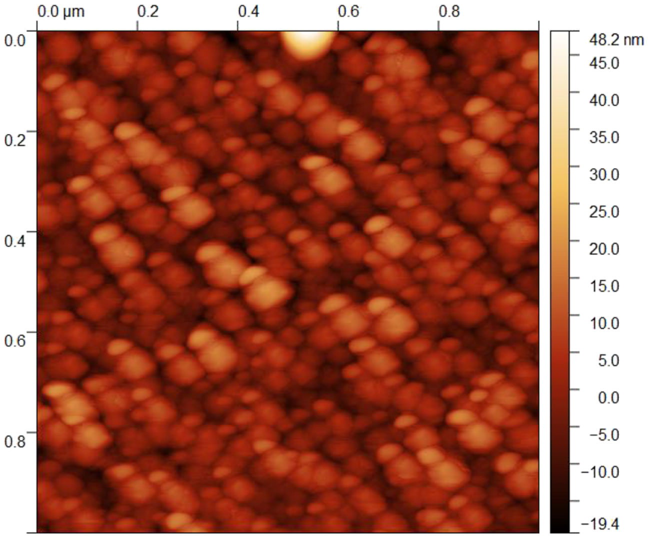

Figure 4. AFM image of a thin film of $Ag@Ag_2O$ NPs with a specific way of self-order.

Regarding the size and shape of NPs, as the AFM images confirm, $Ag@Ag_2O$ NPs are more uniform in comparison to the bare Ag ones. According to the size distribution functions of NPs (Figure 5a,b) the most probable radius of bare Ag NPs belongs to the range from 10 to 15 nm, while $Ag@Ag_2O$ NPs are a bit larger with the most probable cumulative radius ranging from 15 to 20 nm. These results are in excellent agreement with the ones obtained from XRD analysis. The phase AFM images (i.e., the phase contrast images generated on the basis of the lag between the signal driving the cantilever oscillations and the output signal, reflecting the changes in mechanical properties of different segments of the surface) also go with the core−shell structure type of observed NPs, excluding presence of two phases on the surface.

In addition to the fact that ultrasonic irradiation influences the reaction mechanism, it is obvious from the presented AFM images that sonication of the reaction system influences the way of ordering of NPs on the substrate surface leading to deposition of thin films with smaller roughness.

Aside from affecting the composition of the final product and the average nanocrystal size, sonication of the reaction system can also affect the particle size distribution. As the acoustic wavelengths are notably higher than the molecular dimensions, the sonication impact on the reactor consists of a set of indirect effects. However, the most notable one is the acoustic cavitation. If the ultrasound amplitude at a given frequency falls above the cavitation threshold, local hydrostatic pressure variations cause sequential formation and oscillation of bubbles followed by their collapse (implosion). As a consequence of the transient character of the bubbles' implosion, the locally stored energy of the acoustic field is released, causing local temperatures as high as ∼5000 K and pressures of the order of ∼1 kbar. Such primary sonochemical effects create localized reactor conditions that have substantial chemical effects. As the oscillating bubbles can grow up to a certain size limit, the primary sonochemical reaction sites have a relatively narrow size distribution, which usually results in a limited size dispersion of the synthesized NPs and a narrower size distribution. The secondary sonochemical effects under heterogeneous sonochemical conditions, which arise from generation of microjects and shockwaves right after bubbles'

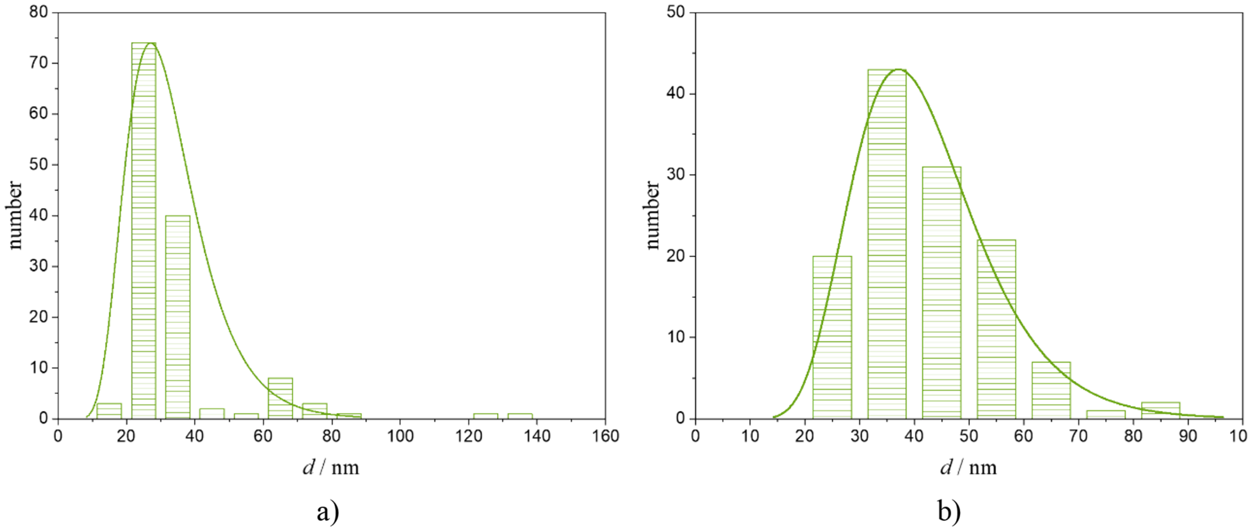

Figure 5. Size distribution of (a) Ag NPs and (b) Ag@ Ag_2O NPs.

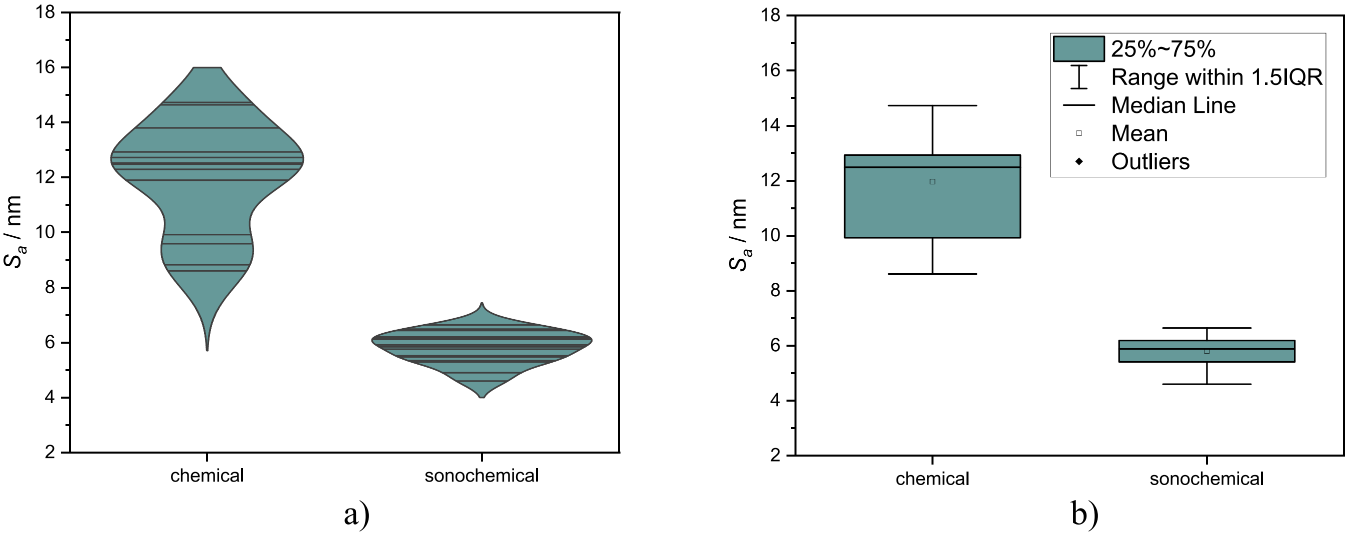

Figure 6. Violin (a) and box (b) plots of the calculated values of S_q for a series of thin-film specimens prepared by the chemical and sonochemical approaches.

implosion, often prevent further crystal growth and agglomeration processes, resulting again in a narrower size distribution of the synthesized NPs. In the present study, the sonication of the reactor causes a substantial change in the reaction mechanism, resulting in a different product as compared to the non-sonicated case. It is therefore not possible to make reliable comparisons of NP size distributions in the two cases currently studied. However, we do observe a much narrower size distribution of the core−shell NPs in the present study, as compared to our previous results obtained with a conventional (non-sonicated) reaction system.[25]

3.3.1. Quantitative AFM Image Analysis. More in-depth physical insights into the topology of prepared surfaces have been gained by advanced analysis of their real- and reciprocal-space statistical characteristics.

The essential first-order real-space statistical property that was considered is the interface width (w), also known as the rms (root mean square) roughness of the film (S_q). If the AFM image contains a 2D field of $N_x \times N_y$ points, w is defined as[36,37]

$$S_q = \sqrt{\frac{1}{N_x N_y}\sum_{i=1}^{N_x}\sum_{j=1}^{N_y}[h(i,j) - \langle h(i,j)\rangle]^2} \tag{21}$$

where $\langle h(i, j)\rangle$ denotes the surface height expectation value (arithmetic mean):

$$\langle h(i,j)\rangle = \frac{1}{N_x N_y}\sum_{i=1}^{N_x}\sum_{j=1}^{N_y} h(i,j) \tag{22}$$

The calculated values of S_q for a series of thin-film specimen synthesized from sonicated and unsonicated reaction systems are presented in Figure 6 with violin plots as well as with the box charts (Figure S1 from the Supporting Information shows analogous plots for the mean roughness values). Notable differences between the two populations are evident from the two types of plots already. Both the interface width and the mean roughness are significantly smaller for surfaces synthesized by the sonochemical approach as compared to those obtained by the conventional colloidal route. At the same time, the dispersion of the two parameters is significantly smaller in the former case as well. The differences in the mean S_q and S_a values for the two data series were shown to be statistically significant using the two-sample t-test (under assumption of both equal and non-equal variances), as well as by the Hotelling's T-squared two-sample tests.

The calculated data for the first-order statistics parameters related to surface topology, the average roughness (S_a), and the root mean square roughness (S_q) are shown in Table 2.

Table 2. Roughness of Thin Films Composed of Ag and Ag_2O@Ag NPs

thin film of close-packed	S_a (nm)	S_q (nm)
Ag NPs	12.87 ± 0.37	16.08 ± 0.47
Ag@Ag_2O NPs	5.86 ± 0.21	7.40 ± 0.36

Significant changes in the surface morphology of the films synthesized by the two developed routes could be also seen from the second-order statistical properties of the AFM images.[39,40] We hereby rely on the most frequently used one-dimensional variant of the full 2D autocorrelation function (ACF) defined as a cut along the fast-scan direction:[41]

$$A(r = md) = A(m, 0) = \frac{1}{N_y\cdot(N_x - m)\cdot w^2}\sum_{j=1}^{N_y}\sum_{i=1}^{N_x-m} h(i+m, j)\cdot h(i, j) \tag{23}$$

Typical $A(r)$ plots for the studied thin films are shown in Figure 7.

As it is obvious from the trends in the $A(r)$ dependencies, the surfaces produced by the chemical route are self-affine, while those synthesized from the ultrasonically irradiated reaction systems have a mounded structure (as seen from the oscillatory behavior manifested at higher r values, usually higher than the lateral correlation length ξ).[42−51] To quantitatively test the self-affine characteristics of the chemically deposited surfaces, as well as to extract numerical estimations of the relevant parameters quantifying these characteristics, the corresponding ACFs have been fitted with model functions of self-affine form:

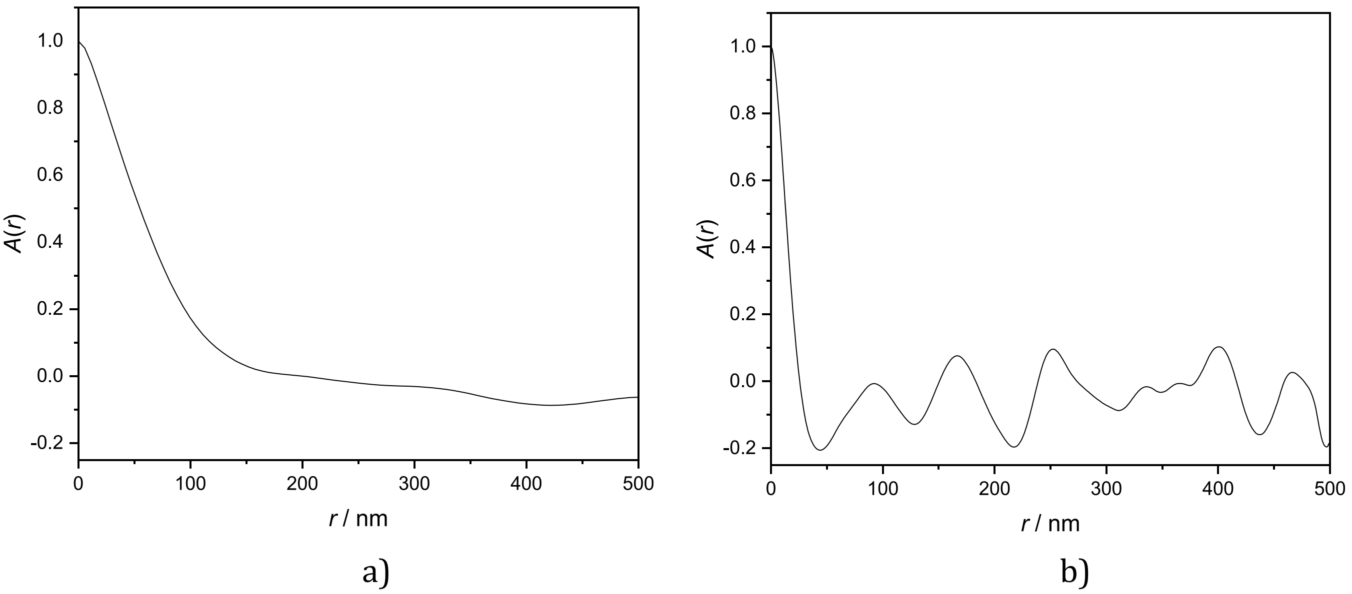

Figure 7. The autocorrelation function for thin films deposited by chemical (a) and sonochemically assisted (b) routes.

$$A(r) = \exp\left[-\left(\frac{r}{\xi}\right)^{2a}\right] \quad (24)$$

Typical fit of an ACF for chemically deposited films with model function of the self-affine form (24) is shown in Figure S2 in the Supporting Information. The values of the Hurst exponent a and lateral correlation length ξ, obtained by non-linear least-square fitting procedure, are given in Table 3. The results obtained in the present study are noticeably different from those reported in our previous work related to $CuInS_2$ QDs deposited as thin films.[27,42] In the case of $CuInS_2$ QD films, a mound to self-affine transition of the surface morphology was evidenced upon ultrasonic treatment of the reactor. Such behavior was essentially attributed to the heterogeneous sonochemical effects.[42] In the present work, however, the situation is quite the opposite. Ultrasonic irradiation here induces the mounded character. This is due to the more substantial change of mechanism induced by the ultrasound in the present study. A direct consequence of the different reaction path is the change of the chemical composition of the surface. The Hurst exponent is higher in the case of sonochemically deposited films, approaching the value characterizing the Gaussian form of the ACF. At the same time, the lateral correlation length is more than three times lower in sonochemically deposited films as compared to the chemically deposited ones.

Table 3. Values of the Parameters a and ξ of an ACF for Chemically Deposited Film and the Sonochemically Deposited Surfaces (at Small Length Scales), Obtained by Non-Linear Least-Square Fitting of the Experimental Data with Model Function of the Self-Affine Form (Eq 24)

thin film of close-packed	a	ξ (nm)
Ag NPs	0.68 ± 0.07	72.98 ± 4.06
$Ag@Ag_2O$ NPs	0.93 ± 0.01	18.98 ± 0.09

As a further proof of the mounded character of the sonochemically deposited films, Figure S3 given in the Supporting Information shows a plot of the power spectral density function (PSDF), computed as Fourier transformation of the 1D ACF:

$$P(k_{\|}) = \frac{1}{2\pi}\int_{-\infty}^{+\infty} A(r)\exp(-ik_{\|}r)\mathrm{d}r \quad (25)$$

It exhibits a well-defined peak appearing at about 1.5×10^8 nm^{-1}, which supports the conclusions concerning the mounded character of the surface, implied by the long-range behavior of the ACF.

3.4. UV–Vis Measurements: Evidence for the LSPR Phenomenon and Its Modification under Ultrasonic Irradiation of the Reaction System.

The phenomenon of LSPR involves coherent oscillations of surface conduction electrons, which are induced by interaction with the external electromagnetic field.[52−63] Considering the potential applicability of the synthesized nanomaterials, LSPR plays an exceptional role. We have therefore paid a more focused attention to this phenomenon in the present study. In fact, several material-related factors determine the LSPR effect spectral characteristics. These include the material of which the nanocrystals are built up as well as their size and shape, along with the size distribution and the refractive index of their immediate surroundings.[52−67]

Figure 8a,b shows normalized absorption spectra of thin-film specimens composed of bare Ag NPs and $Ag@Ag_2O$ core−shell NPs with different silver core radii and a silver oxide shell thickness in the spectral region from ∼300 to 1000 nm. Since scattering of the used incident electromagnetic radiation by these nanostructures is very small compared to absorption, the absorption and extinction are approximately equal[25] and either of these two physical quantities can be used further on in a quantitative analysis of the optical spectroscopy data.

As can be seen from Figure 8, both Ag and $Ag@Ag_2O$ NP-based thin films exhibit surface plasmon resonance in the visible region. The appearance of only one absorption maximum strongly suggests that the shape of synthesized NPs is close to spherical. On the other hand, obvious differences between presented absorption spectra can be noticed. Regarding the thin film of self-assembled Ag NPs (Figure 8a), the maximum plasmon enhancement is reached at

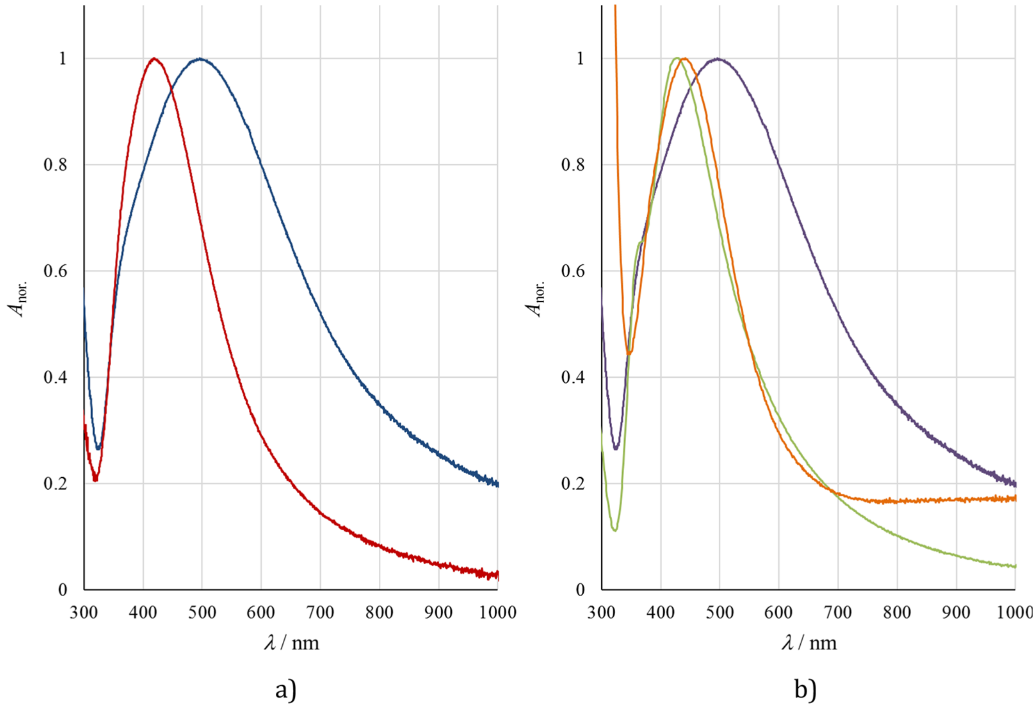

Figure 8. Normalized absorption spectra of thin films built up by (a) Ag bare NPs (red line) and Ag@Ag$_2$O NPs (blue line) and (b) Ag@Ag$_2$O NPs with different core radii and shell thickness (in the order of increase of $\lambda_{max.}$: core 4.8 nm, shell 8.8 nm; core 5.0 nm, shell 9.0 nm; and core 5.3 nm, shell 9.5 nm).

~419 nm. The observed plasmon resonance wavelength strongly depends on the radius of Ag NP (~9 nm according to XRD analysis).[7,8,25,62,64] Secondly, the full width at half maximum (FWHM) of the absorption peak is inversely proportional to the NP size[24,64−75] when one compares spectra of NPs of the same material with the same geometrical characteristics.

Regarding the thin films composed of self-assembled core−shell nanostructures, as Figure 8 confirms, the plasmon resonance wavelength is red shifted compared with bare Ag NP-based thin films. Also, this quantity is strongly influenced by geometrical characteristics of Ag@Ag$_2$O NPs: the core radius, the thickness of the shell, and the ratio between them.[24,68−81] As the shell/core ratio increases, the red shift of the plasmon resonance wavelength becomes larger (Figure 8b). In addition to this, the geometrical features of Ag@Ag$_2$O NPs determine the FWHM of the resonance absorption peak, i.e., the broadening of the absorption peak decreases as the core radius increases, while it becomes more notable as the shell thickness increases. The increasing contrast, defined as $C = (I_{max} - I_{min})/I_{max}$ (where I_{min} is taken around $\lambda_{min} = 320$ nm), changes with the increase of the core radius and shell thickness. The discussed experimental observations are in excellent agreement with the published quantitative models for sizing Ag@Ag$_2$O core−shell structures on the basis of their optical properties.[25,78]

Also, the influence of self-assembly of NPs (i.e., plasmon coupling) on the absorption spectra, especially in the range of larger wavelengths, cannot be neglected.[65,66] This might be due to the different way of self-assembly of bare Ag NPs, on the one hand, and core−shell Ag@Ag$_2$O nanostructures on the other hand, a fact that has been noticed on the basis of results obtained from AFM measurements.

To get an in-depth understanding of the LSPR-related issues, a more thorough analysis of the experimental UV−vis spectra has been carried out along with modeling based primarily on Mie's theory and its modifications and adaptations to nanostructures.[68−75] Assuming monodispersed Ag nanocrystals with a size-modified complex dielectric constant of the form

$$\varepsilon_{Ag}^{mod}(\omega) = \varepsilon_{Ag}^{bulk}(\omega) + \frac{\Omega_p^2}{\omega(\omega + i\tau_{bulk}^{-1})} - \frac{\Omega_p^2}{\omega(\omega + i\tau_{mod}^{-1})} \tag{26}$$

(where Ω_p is the Drude plasma frequency of the conduction electrons in Ag), Mie's theory predicts a rather narrow LSPR band, which exhibits a small red shift from 356 to 361 nm upon crystal size increase from 9 to 20 nm, which is far below the experimentally observed value. To get a good agreement with the experimental data, it is necessary to include both the dispersion in the size distribution of the metallic NPs (which induces an inhomogeneous broadening of the LSPR band) and the effect of the substrate. Within the effective medium approach, the effective refractive index depends on value characteristic for the medium n_m (in our case air, or a mixture of the air and proximal Ag NPs)[76−82] as well as the value characteristic for the substrate n_s:

$$n_{eff} = \beta n_m + (1 - \beta) n_s \tag{27}$$

while β is a weighting factor. In the so-called geometrical effective medium approximation (GEMA), the effective dielectric permittivity reduces to the arithmetic mean of the medium and substrate values. We have further proceeded with simulations of the LSPR band shapes within the framework of the effective medium approach. In Figure 9a, the evolution of the LSPR peak shape with the increase of the size dispersion for a nanocrystalline film characterized with an average size of

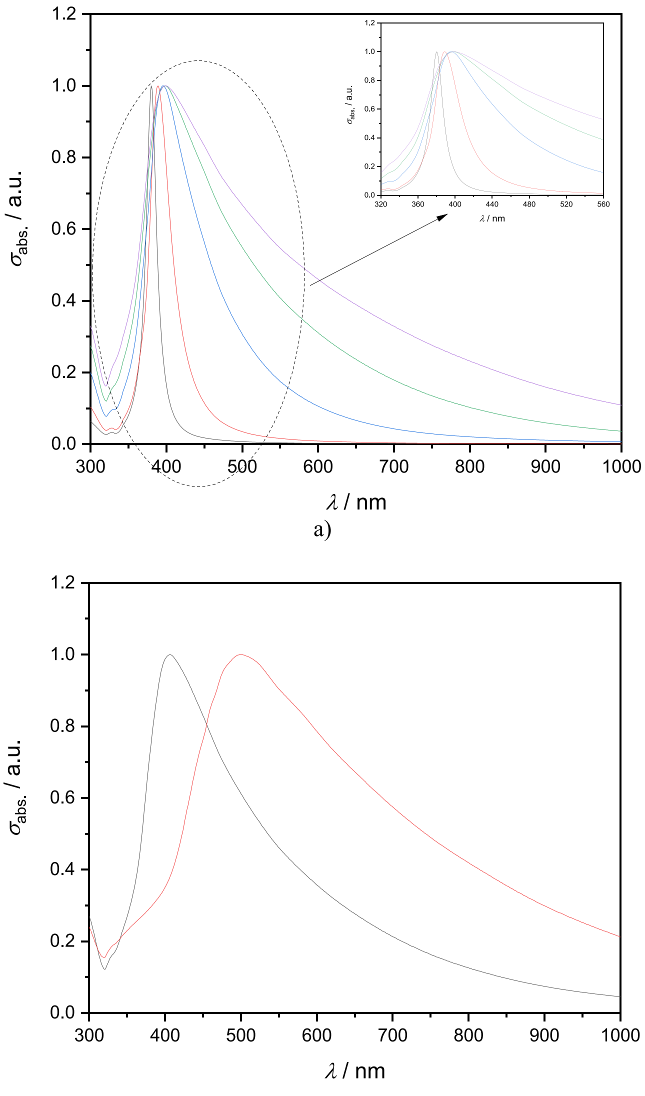

a)

b)

Figure 9. (a) Evolution of the LSPR peak shape with the increase of the size dispersion for a nanocrystalline film characterized with the average size of Ag NPs of 9 nm placed with an effective medium with refractive index 1.27 (see text for more details); LSPR spectra are represented as dependencies of absorption cross section on the wavelength of the incident photons. (b) The LSPR bands for Ag and Ag@Ag_2O NP films simulated by Mie's theory; the resemblance of the experimental data is excellent.

Ag NPs of 9 nm placed with an effective medium with refractive index 1.27 is shown. As can be seen, the apparent shift of the peak maximum up to about 400 nm and the inhomogeneous broadening and asymmetry to the high-wavelength side observed in our experiments are excellently reproduced by these two effects. Therefore, the actual appearance of the LSPR spectrum in our present case can be ascribed to a complex interplay between the change in the effective medium dielectric permittivity (as a consequence of interdot coupling and the influence of the substrate) and the size dispersion of the colloidally deposited Ag NPs.

When the Ag NPs are embedded in a shell of silver oxide (Ag@Ag_2O), the experimental LSPR peak exhibits a large shift by about 90 nm. Such shift can be rather accurately predicted by Mie's theory, using the range of values for the optical constants of Ag_2O reported in the literature.[83,84] In Figure 9b, the LSPR bands for Ag and Ag@Ag_2O NP films simulated by Mie's theory are shown. The resemblance of the experimental data shown in Figure 8a is excellent.

4. CONCLUSIONS

In summary, in the present paper, we have developed a controllable ultrasound-assisted synthetic approach based on a colloidal reaction system that allows deposition of nanoplasmonic surfaces built up by elemental silver nanocrystals (in the absence of ultrasonic irradiation) or core−shell Ag@Ag_2O NPs (under sonochemical conditions). A detailed elaboration of the reaction mechanism is provided along with an argumentation, showing that ultrasonic irradiation of the reaction system induces substantial changes in the reaction mechanism, hence changing the reaction channel and opening the possibility for product control. Both the Scherrer's and the Williamson−Hall's approaches consistently estimate a value of ∼9 nm for the average NP size in the case of bare Ag films. According to Scherrer's approach, in the case of Ag@Ag_2O core−shell nanoplasmonics, the average size of the Ag core is ∼5 nm, while the thickness of the Ag_2O shell is ∼9 nm. XRD data are consistent with the AFM observations. As revealed by analysis of the first-order statistical properties of the synthesized nanoplasmonic surfaces, both the interface width and the mean roughness are significantly smaller for surfaces synthesized by the sonochemical approach as compared to those obtained by the conventional colloidal route. The dispersion of the two parameters is significantly smaller in the former case as well, the differences in the mean S_q and S_a values for the two data series being statistically significant. As shown by analysis of the second-order statistical parameters, the chemically deposited films exhibit self-affine properties, while ultrasonic irradiation of the reaction system alters this completely so that the sonochemically obtained films are mounded. Optical properties of the synthesized materials are dominated by the localized surface plasmon absorption. The observed trends were rationalized on the basis of Mie's theory and its modifications. We have found out that the actual spectral appearance in the UV−vis spectral range is governed by several factors, the most important of which are particle size, size dispersion-induced inhomogeneous broadening, plasmonic coupling between proximal NPs, and the interaction of the nanostructures with the glass substrate. The most notable shift of the LSPR absorption maximum in the case of Ag@Ag_2O core−shell NPs as compared to the bare Ag ones was, however, found to be induced by the influence of the dielectric Ag_2O shell.

■ ASSOCIATED CONTENT

SI Supporting Information

The Supporting Information is available free of charge at https://pubs.acs.org/doi/10.1021/acs.jpcc.3c01267.

> Discussion concerning the complexing versus reduction properties of TEA; plots related to Scherrer's and Williamson−Hall's analyses of X-ray diffraction data; the calculated mean roughness values (S_a) for a series of thin-film specimen synthesized from sonicated and unsonicated reaction systems presented with violin plots as well as with the box charts; plots related to the second-order statistical properties calculated on the basis of AFM data for the studied films (PDF)

AUTHOR INFORMATION

Corresponding Author

Biljana Pejova – *Institute of Chemistry, Faculty of Natural Sciences and Mathematics, SS. Cyril and Methodius University, 1000 Skopje, Macedonia; Department of Mechanical and Structural Engineering and Materials Science, Faculty of Science and Technology, University of Stavanger, 4036 Stavanger, Norway;* orcid.org/0000-0003-4670-6669; Email: biljana@pmf.ukim.mk

Authors

Simona Premcheska – *Institute of Chemistry, Faculty of Natural Sciences and Mathematics, SS. Cyril and Methodius University, 1000 Skopje, Macedonia; Department of Chemistry, Ghent University, 9000 Ghent, Belgium;* orcid.org/0000-0002-0372-339X

Emel Sherif Miftar – *Institute of Chemistry, Faculty of Natural Sciences and Mathematics, SS. Cyril and Methodius University, 1000 Skopje, Macedonia*

Complete contact information is available at: https://pubs.acs.org/10.1021/acs.jpcc.3c01267

Notes

The authors declare no competing financial interest.

ACKNOWLEDGMENTS

B.P. acknowledges the support from the Ministry of Science and Education of the Republic of North Macedonia (grant 15-15590/38) for strengthening the research capacity of the Laboratory for Nanomaterials.

REFERENCES

(1) Boltasseva, A.; Atwater, H. A. Low-loss plasmonic metamaterials. *Science* **2011**, *331*, 290−291.

(2) Naik, G. V.; Shalaev, V. M.; Boltasseva, A. Alternative plasmonic materials: beyond gold and silver. *Adv. Mater.* **2013**, *25*, 3264−3294.

(3) Mirkin, C. A.; Letsinger, R. L.; Mucic, R. C.; Storhoff, J. J. A DNA-based method for rationally assembling nanoparticles into macroscopic materials. *Nature* **1996**, *382*, 607−609.

(4) Elghanian, R.; Storhoff, J. J.; Mucic, R. C.; Letsinger, R. L.; Mirkin, C. A. Selective colorimetric detection of polynucleotides based on the distance-dependent optical properties of gold nanoparticles. *Science* **1997**, *277*, 1078−1081.

(5) Quinten, M.; Leitner, A.; Krenn, J. R.; Aussenegg, F. R. Electromagnetic energy transport via linear chains of silver nanoparticles. *Opt. Lett.* **1998**, *23*, 1331−1333.

(6) Brongersma, M. L.; Hartman, J. W.; Atwater, H. A. Electromagnetic energy transfer and switching in nanoparticle chain arrays below the diffraction limit. *Phys. Rev. B* **2000**, *62*, 16356−16359.

(7) Kelly, K. L.; Coronado, E.; Zhao, L. L.; Shatz, G. C. The optical properties of metal nanoparticles: the Influence of size, shape and dielectric environment. *J. Phys. Chem. B* **2003**, *107*, 668−677.

(8) Ghosh Chaudhuri, R.; Paria, S. Core/shell nanoparticles: classes, properties, synthesis mechanisms, characterization and applications. *Chem. Rev.* **2012**, *112*, 2373−2433.

(9) Balakrishnan, S.; Bonder, M. J.; Hadjipanayis, G. C. Particle size effect on phase and magnetic properties of polymer-coated magnetic nanoparticles. *J. Magn. Magn. Mater.* **2009**, *321*, 117−122.

(10) Laurent, S.; Forge, D.; Port, M.; Roch, A.; Robic, C.; Elst, L. V.; Muller, R. N. Magnetic iron oxide nanoparticles: synthesis, stabilization, vectorization, physicochemical characterizations and biological applications. *Chem. Rev.* **2008**, *108*, 2064−2110.

(11) Salgueiriño-Maceira, V.; Correa-Duarte, M. A. Increasing the complexity of magnetic core/shell structured nanocomposites for biological applications. *Adv. Mater.* **2007**, *19*, 4131−4144.

(12) Dresco, P. A.; Zaitsev, V. S.; Gambino, R. J.; Chu, B. Preparation and properties of magnetite and polymer magnetite nanoparticles. *Langmuir* **1999**, *15*, 1945−1951.

(13) Yan, E.; Ding, Y.; Chen, C.; Li, R.; Hu, Y.; Jiang, X. Polymer/silica hybrid hollow nanospheres with pH-sensitive drug release in physiological and intracellular environments. *Chem. Commun.* **2009**, *19*, 2718−2720.

(14) Michalet, X.; Pinaud, F. F.; Bentolila, L. A.; Tsay, J. M.; Doose, S.; Li, J. J.; Sundaresan, G.; Wu, A. M.; Gambhir, S. S.; Weiss, S. Quantum dots for live cells, in vivo imaging and diagnostics. *Science* **2005**, *307*, 538−544.

(15) De, M.; Ghosh, P. S.; Rotello, V. M. Applications of nanoparticles in biology. *Adv. Mater.* **2008**, *20*, 4225−4241.

(16) Zhao, D.; Feng, J.; Huo, Q.; Melosh, N.; Fredrickson, G. H.; Chmelka, B. F.; Stucky, G. D. Triblock copolymer syntheses of mesoporous silica with periodic 50 to 300 Angstrom Pores. *Science* **1998**, *279*, 548−552.

(17) Li, J.-F.; Tian, X. D.; Li, S. B.; Anema, J. R.; Yang, Z. L.; Ding, Y.; Wu, Y. F.; Zeng, Y. M.; Chen, Q. Z.; Ren, B.; Wang, Z. L.; Tian, Z. Q. Surface analysis using shell-isolated nanoparticle-enhanced Raman spectroscopy. *Nat. Protoc.* **2013**, *8*, 52−65.

(18) Langer, J.; Jimenez de Aberasturi, D.; Aizpurua, J.; Alvarez-Puebla, R. A.; Auguié, B.; Baumberg, J. J.; Bazan, G. C.; Bell, S. E. J.; Boisen, A.; Brolo, A. G.; et al. Present and future of surface-enhanced Raman scattering. *ACS Nano* **2020**, *14*, 28−117.

(19) Li, J.-F.; Zhang, Y.-J.; Ding, S.-Y.; Panneerselvam, R.; Tian, Z.-Q. Core-shell nanoparticle-enhanced Raman spectroscopy. *Chem. Rev.* **2017**, *117*, 5002−5069.

(20) Li, J.-F.; Li, C.-Y.; Aroca, R. F. Plasmon-enhanced fluorescence spectroscopy. *Chem. Soc. Rev.* **2017**, *46*, 3962−3979.

(21) Li, J.-F.; Huang, Y. F.; Ding, Y.; Yang, Z. L.; Li, S. B.; Zhou, X. S.; Fan, F. R.; Zhang, W.; Zhou, Z. Y.; Wu, D. Y.; et al. Shell-isolated nanoparticle-enhanced Raman spectroscopy. *Nature* **2010**, *464*, 392−395.

(22) Pejova, B.; Grozdanov, I.; Nesheva, D.; Petrova, A. Size-dependent properties of sonochemically synthesized three-dimensional arrays of close-packed semiconducting $AgBiS_2$ quantum dots. *Chem. Mater.* **2008**, *20*, 2551−2565.

(23) Pejova, B.; Nesheva, D.; Aneva, Z.; Petrova, A. Photoconductivity and relaxation dynamics in sonochemically synthesized assemblies of $AgBiS_2$ quantum dots. *J. Phys. Chem. C* **2011**, *115*, 37−46.

(24) Schinca, D. C.; Scaffardi, L. B.; Videla, F. A.; Torchia, G. A.; Moreno, P.; Roso, L. Silver-silver oxide core-shell nanoparticles by femtosecond laser ablation: core and shell sizing by extinction spectroscopy. *J. Phys. D: Appl. Phys.* **2009**, *42*, 215102−215111.

(25) Santillán, J. M. J.; Scaffardi, L. B.; Schinca, D. C. Quantitative optical extinction-based parametric method for sizing a single core−shell Ag−Ag_2O nanoparticle. *J. Phys. D: Appl. Phys.* **2011**, *44*, 105104−105112.

(26) Elechiguerra, J. L.; Burt, J. L.; Morones, J. R.; Camacho-Bragado, A.; Gao, X.; Lara, H. H.; Yacaman, M. J. Interaction of silver nanoparticles with HIV-1. *J. Nanobiotechnol.* **2005**, 3, 1−10.

(27) Pejova, B.; Sherif, E.; Minde, M. W. Sonochemically synthesized quantum nanocrystals of cubic $CuInS_2$: Evidence for multifractal surface morphology, size-dependent structure and particle size distribution. *J. Phys. Chem. C* **2020**, *124*, 20240−20255.

(28) Nečas, D.; Klapetek, P. Gwyddion: An open-source software for SPM data analysis. *Cent. Eur. J. Phys.* **2012**, *10*, 181−188.

(29) Rumble, J. *CRC Handbook of chemistry and physics*; 102nd ed.; CRC Press, 2021-2022.

(30) Kocareva, T.; Grozdanov, I.; Pejova, B. Ag and AgO thin film formation in Ag^+−triethanolamine solutions. *Mater. Lett.* **2001**, *47*, 319−323.

(31) Xu, H.; Zeiger, B. W.; Suslick, K. S. Sonochemical synthesis of nanomaterials. *Chem. Soc. Rev.* **2012**, *42*, 2555−2567.

(32) Ye, Z.; Li, C.; Chen, Q.; Xu, Y.; Bell, S. E. J. Self-assembly of colloidal nanoparticles into 2D arrays at water-oil interfaces: rational construction of stable SERS substrates with accessible enhancing

surfaces and tailored plasmonic response. *Nanoscale* **2021**, *13*, 5937−5953.

(33) Wu, Z.; Yao, Q.; Zang, S.; Xie, J. Directed self-assembly of ultrasmall metal nanoclusters. *ACS Mater. Lett.* **2019**, *1*, 237−248.

(34) Kolay, S.; Bain, D.; Maity, S.; Devi, A.; Patra, A.; Antoine, R. Self-assembled metal nanoclusters: Driving forces and structural correlation with optical properties. *Nanomaterials* **2022**, *12*, 544.

(35) Open-access collection of crystal structures of organic, inorganic, metal-organic compounds and minerals, Department of Chemistry, University of Cambridge.

(36) Williamson, G. K.; Hall, W. H. X-ray line broadening from filed aluminium and wolfram. *Acta Metall.* **1953**, *1*, 22−31.

(37) Suryanarayana, C.; Grant Norton, M. *X-ray diffraction: a practical approach*; Springer: New York, 1998.

(38) Mote, V. D.; Purushotham, Y.; Dole, B. N. Williamson-Hall analysis in estimation of lattice strain in nanometer-sized ZnO particles. *J. Theor. Appl. Phys.* **2012**, *6*, 1−8.

(39) Nečas, D.; Valtr, M.; Klapetek, P. How levelling and scan line corrections ruin roughness measurement and how to prevent it. *Sci. Rep.* **2020**, *10*, 15294.

(40) Nečas, D.; Klapetek, P.; Valtr, M. Estimation of roughness measurement bias originating from background subtraction. *Meas. Sci. Technol.* **2020**, *31*, No. 094010.

(41) Nečas, D.; Klapetek, P. One-dimensional autocorrelation and power spectrum density functions of irregular regions. *Ultramicroscopy* **2013**, *124*, 13−19.

(42) Pejova, B. Ultrasound driven mound to self-affine surface structure transition in nanostructured films: one-pot route to cubic cuins$_2$ quantum dots with controlled structure and tunable band gap energy. *J. Mater. Sci.: Mater. Electron.* **2019**, *30*, 12679−12694.

(43) Aguilar, M.; Anguiano, E.; Aznárez, J. A.; Sacedón, J. L. Rough growth fronts of evaporated gold films, compared with self-affine and mound growth models. *Surf. Sci.* **2001**, *482-485*, 935−939.

(44) Raoufi, D. Morphological characterization of ITO thin films surfaces. *Appl. Surf. Sci.* **2009**, *255*, 3682−3686.

(45) Osafo-Acquaah, A.; Shapir, Y.; Jorne, J. Transition in surface growth from self-affine to mounds during copper electrodeposition. *J. Electrochem. Soc.* **2006**, *153*, C535−C539.

(46) Pellicione, M.; Lu, T.-M. *Evolution of thin film morphology: modeling and simulations*; Springer-Verlag: Berlin-Heidelberg, 2008.

(47) Das Sarma, S.; Punyindu, P.; Toroczkai, Z. Non-universal mound formation in non-equilibrium surface growth. *Surf. Sci. Lett.* **2000**, *457*, L369−L375.

(48) Das Sarma, S.; Punyindu, P. A discrete model for non-equilibrium growth under surface diffusion bias. *Surf. Sci. Lett.* **1999**, *424*, L339−L346.

(49) Kahanda, G. L. M. K. S.; Zou, X.-Q.; Farrell, R.; Wong, P. Columnar growth and kinetic roughening in electrochemical deposition. *Phys. Rev. Lett.* **1992**, *68*, 3741−3744.

(50) Iwamoto, A.; Yoshinobu, T.; Iwasaki, H. Kinetic roughening in electrodissolution of copper. *Phys. Rev. E* **1999**, *59*, 5133−5136.

(51) Krug, J.; Plischke, M.; Siegert, M. Surface diffusion currents and the universality classes of growth. *Phys. Rev. Lett.* **1993**, *70*, 3271−3274.

(52) Zheng, J.; Cheng, X.; Zhang, H.; Bai, X.; Ai, R.; Shao, L.; Wang, J. Gold Nanorods: The most versatile plasmonic nanoparticles. *Chem. Rev.* **2021**, *121*, 13342−13453.

(53) Pathak, N. K.; Ji, A.; Sharma, R. P. Tunable properties of surface plasmon resonances: the influence of core-shell thickness and dielectric environment. *Plasmonics* **2014**, *9*, 651−657.

(54) Zheng, P.; Tang, H.; Liu, B.; Kasani, S.; Huang, L.; Wu, N. Origin of strong and narrow localized surface plasmon resonance of copper nanocubes. *Nano Res.* **2019**, *12*, 63−68.

(55) Luther, J. M.; Jain, P. K.; Ewers, T.; Alivisatos, A. P. Localized surface plasmon resonances arising from free carriers in doped quantum dots. *Nat. Mater.* **2011**, *10*, 361−366.

(56) Willets, K. A.; Van Duyne, R. P. Localized surface plasmon resonance spectroscopy and sensing. *Annu. Rev. Phys. Chem.* **2007**, *58*, 267−297.

(57) Sayed, M.; Yu, J.; Liu, G.; Jaroniec, M. Non-noble plasmonic metal-based photocatalysts. *Chem. Rev.* **2022**, *122*, 10484−10537.

(58) Hutter, E.; Fendler, J. H. Exploitation of localized surface plasmon resonance. *Adv. Mater.* **2004**, *16*, 1685−1706.

(59) Fong, K. E.; Yung, L.-Y. L. Localized surface plasmon resonance: a unique property of plasmonic nanoparticles for nucleic acid detection. *Nanoscale* **2013**, *5*, 12043−12071.

(60) Olson, J.; Dominguez-Medina, S.; Hoggard, A.; Wang, L.-Y.; Chang, W.-S.; Link, S. Optical characterization of single plasmonic nanoparticles. *Chem. Soc. Rev.* **2015**, *44*, 40−57.

(61) Gibbs, S. L.; Staller, C. M.; Agrawal, A.; Johns, R. W.; Saez Cabezas, C. A.; Milliron, D. J. Intrinsic optical and electronic properties from quantitative analysis of plasmonic semiconductor nanocrystal ensemble optical extinction. *J. Phys. Chem. C* **2020**, *124*, 24351−24360.

(62) Mayer, K. M.; Hafner, J. H. Localized surface plasmon resonance sensors. *Chem. Rev.* **2011**, *111*, 3828−3857.

(63) Lin, J.-S.; Radjenovic, P. M.; Jin, H.; Li, J.-F. Plasmonic core-shell nanoparticle enhanced spectroscopies for surface analysis. *Anal. Chem.* **2021**, *93*, 6573−6582.

(64) Zhao, L.; Kelly, K. L.; Schatz, G. C. The Extinction Spectra of Silver Nanoparticle Arrays: Influence of array structure on plasmon resonance wavelength and width. *J. Phys. Chem. B* **2003**, *107*, 7343−7350.

(65) Ghosh, S. K.; Pal, T. Interparticle coupling effect on the surface plasmon resonance of gold nanoparticles: from theory to applications. *Chem. Rev.* **2007**, *107*, 4797−4862.

(66) Grand, J.; Auguié, B.; Le Ru, E. C. Combined extinction and absorption uv-visible spectroscopy as a method for revealing shape imperfections of metallic nanoparticles. *Anal. Chem.* **2019**, *91*, 14639−14648.

(67) Kolwas, K.; Derkachova, A.; Shopa, M. Size characteristics of surface plasmons and their manifestation in scattering properties of metal particles. *J. Quant. Spectrosc. Rad. Transfer* **2009**, *110*, 1490−1501.

(68) Bohren, C. F.; Huffman, D. R. *Absorption and scattering of light by small particles*; Wiley-Interscience: New York, NY, USA, 1998.

(69) Mishchenko, M. I.; Travis, L. D.; Lacis, A. A. *Scattering, absorption and emission of light by small particles*; Cambridge University Press: Cambridge, UK, 1st ed.; 2002.

(70) Pena-Rodriguez, O.; Gonzales Perez, P. P.; Pal, U. MieLab: A software tool to perform calculations on the scattering of electromagnetic waves by multilayered spheres. *Int. J. Spectrosc.* **2011**, *2011*, No. 583743.

(71) Link, S.; El-Sayed, M. A. Spectral properties and relaxation dynamics of surface plasmon electronic oscillations in gold and silver nanodots and nanorods. *J. Phys. Chem. B* **1999**, *103*, 8410−8426.

(72) Amendola, V.; Meneghetti, M. Size evaluation of gold nanoparticles by uv-vis spectroscopy. *J. Phys. Chem. C* **2009**, *113*, 4277−4285.

(73) Yang, H. U.; D'Archangel, J.; Sundheimer, M. L.; Tucker, E.; Boreman, G. D.; Raschke, M. B. Optical dielectric function for silver. *Phys. Rev. B* **2015**, *91*, No. 235137.

(74) Garcia, M. A.; de la Venta, J.; Crespo, P.; Llopis, J.; Penadés, S.; Fernández, A.; Hernando, A. Surface plasmon resonance of capped Au nanoparticles. *Phys. Rev. B* **2005**, *72*, No. 241403.

(75) Baida, H.; Billaud, P.; Marhaba, S.; Christofilos, D.; Cottancin, E.; Crut, A.; Lermé, J.; Maioli, P.; Pellarin, M.; Broyer, M.; et al. Quantitative determination of the size dependence of surface plasmon resonance damping in Single Ag@SiO$_2$ Nanoparticles. *Nano Lett.* **2009**, *9*, 3463−3469.

(76) Dyck, N. C.; Denomme, R. C.; Nieva, P. M. Effective medium properties of arbitrary nanoparticle shapes in a localized surface plasmon resonance sensing layer. *J. Phys. Chem. C* **2011**, *115*, 15225−15233.

(77) Vernon, K. C.; Funston, A. M.; Novo, C.; Gómez, D. E.; Mulvaney, P.; Davis, T. J. Influence of particle-substrate interaction on localized plasmon resonances. *Nano Lett.* **2010**, *10*, 2080−2086.

(78) Ringe, E.; McMahon, J. M.; Sohn, K.; Cobley, C.; Xia, Y.; Huang, J.; Schatz, G. C.; Marks, L. D.; Van Duyne, R. P. Unraveling the Effects of Size, Composition and substrate on the localized surface plasmon resonance frequencies of gold and silver nanocubes: a systematic single-particle approach. *J. Phys. Chem. C* **2010**, *114*, 12511−12516.

(79) Duval Malinsky, M.; Kelly, K. L.; Schatz, G. C.; Van Duyne, R. P. Nanosphere lithography: effect of substrate on the localized surface plasmon resonance spectrum of silver nanoparticles. *J. Phys. Chem. B* **2001**, *105*, 2343−2350.

(80) Liao, J.; Ji, L.; Zhang, J.; Gao, N.; Li, P.; Huang, K.; Yu, E. T.; Kang, J. Influence of the substrate to the LSP coupling wavelength and strength. *Nanoscale Res. Lett.* **2018**, *13*, 280.

(81) Mahmoud, M. A.; Chamanzar, M.; Adibi, A.; El-Sayed, M. A. Effect of the dielectric constant of the surrounding medium and the substrate on the surface plasmon resonance spectrum and sensitivity factors of highly symmetric systems: silver nanocubes. *J. Am. Chem. Soc.* **2012**, *134*, 6434−6442.

(82) Valamanesh, M.; Borensztein, Y.; Langlois, C.; Lacaze, E. Substrate effect on the plasmon resonance of supported flat silver nanoparticles. *J. Phys. Chem. C* **2011**, *115*, 2914−2922.

(83) Gao, X.-Y.; Feng, H.-L.; Ma, J.-M.; Zhang, Z.-Y. Spectroscopic ellipsometric study of the optical properties of Ag_2O film prepared by direct-current magnetron reactive sputtering. *Chin. Phys. B* **2010**, *19*, No. 090701.

(84) Agasti, S.; Dewasi, A.; Mitra, A. Structural and optical properties of pulse laser deposited Ag_2O thin films. *AIP Conf. Proc.* **2018**, *1953*, No. 060001.

https://doi.org/10.1021/acs.jpcc.3c01267
J. Phys. Chem. C 2023, 127, 11204−11217